Department of Precision and Microsystems Engineering

MEMS Mechanism for Fine-tuning Geometric Anti-Spring Compression

Name

Report no	:	2024.019
Coach	:	Dr. D. (Davood) Farhadi
Professor	:	Prof. dr. M.K. (Murali) Ghatkesar
Specialisation	:	MSD
Type of report	:	Supplementary material Thesis report
Date	:	9 April 2024

Delft University of Technology

Challenge the future

Supplementary material

1 Modelling the geometric anti-springs

1.1 Numerical model

The first model was made using the Euler-Bernoulli beam theory based on the work of Boom et al. [1] and the following elaboration only serves to better describe how we implemented their approach. A schematic depiction of the curved beam is given in Figure 1. First, to generalise the model, the applied loads on the tip (F_x, F_y, T) were normalised:

$$\tau = \frac{L}{EI_z}T, \quad G_i = \frac{L^2}{EI_z}F_i, \quad \text{for } i = x, y, \tag{1}$$

where L is the GAS beam length, E is the (isotropic) Young's Modulus and I_z is the second moment of area around the out-of-plane z-axis. Then, the dimensionless second-order differential equation that was derived for an infinitesimally small part of the beam yielded:

$$\frac{\mathrm{d}^2\theta(p)}{\mathrm{d}p^2} = G_x \sin(\theta(p)) - G_y \cos(\theta(p)), \tag{2}$$

Coordinate p is the normalised coordinate along the length of the beam and goes from 0 to 1 and $\theta(p)$ describes the angle of the beam. To link the displacements in $x(p)$ and $y(p)$ to angle $\theta(p)$, the following relations were used:

$$\frac{x(p)}{L} = \int_0^p \cos(\theta(\xi))\, d\xi, \qquad \frac{y(p)}{L} = \int_0^p \sin(\theta(\xi))\, d\xi \tag{3}$$

To ease solving the above equations, 2 was transformed into two first-order differential equations, and 3 was rewritten into the differential form. Using new dependent variables:

$$z_1 = \theta,\ z_2 = \frac{d\theta}{dp},\ z_3 = \frac{dx}{dp},\ z_4 = \frac{dy}{dp}, \tag{4}$$

the system of equations became:

$$\begin{cases} \frac{dz_1}{dp} = z_2 \\ \frac{dz_2}{dp} = G_x \sin(z_1) - G_y \cos(z_1) \\ \frac{dz_3}{dp} = L\cos(z_1) \\ \frac{dz_4}{dp} = L\sin(z_1) \end{cases} \tag{5}$$

These four equations with the three unknown generalised loads G_x, G_y and τ thus required seven boundary conditions. The first three were obtained from the fixed support at $p = 0$, where the solution should satisfy:

$$x(0) = 0,\ y(0) = 0,\ \theta(0) = \theta_{p0}. \tag{6}$$

Likewise, for $p = 1$, three additional boundary conditions could be be identified:

$$x(1) = x_i(1) - \Delta x,\ y(1) = y_i(1) - \Delta y,\ \theta(1) = \theta_{p1}, \tag{7}$$

where x_i and y_i are the initial coordinates of the beam tip before deformation:

$$\frac{x_i(1)}{L} = \int_0^1 \cos(\theta_i(\xi))\, d\xi,\ \frac{y_i(1)}{L} = \int_0^1 \sin(\theta_i(\xi))\, d\xi, \tag{8}$$

with initial angle:

$$\theta_i(p) = \theta_{p0} - (\theta_{p0} - \theta_{p1})p. \tag{9}$$

The last boundary condition was found by noting that at $p = 1$:

$$\left.\frac{d(\theta - \theta_i)}{dp}\right|_{p=1} = \tau, \tag{10}$$

so:

$$\left.\frac{d\theta}{dp}\right|_{p=1} = \tau - (\theta_{p0} - \theta_{p1}). \tag{11}$$

The system of equations was then solved using SciPy's `solve_bvp` function with the parameters that are listed in Table 1. The value for the Young's modulus was taken to be 156 GPa, which is the average value along the length of the curved beam when the x-axis is in the [110] direction of the silicon crystal [1].

Table 1: GAS dimensions for the G6 accelerometer

Parameter	Symbol	Value
Total spring length	L	[CONFIDENTIAL]
Spring width	w	[CONFIDENTIAL]
Spring height (device Layer height)	t	[CONFIDENTIAL]
Initial angle	θ_{p0}, θ_{p1}	[CONFIDENTIAL]
Isotropic Young's modulus	E	156 GPa

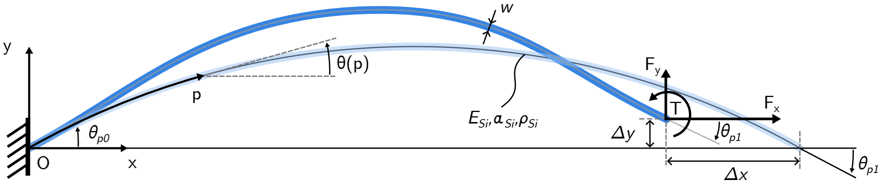

Figure 1: A schematic illustration of the GAS coordinates and dimensions.

1.2 Finite Element Analysis

In order to test the quality of the Euler-Bernoulli beam model, 2D and 3D Finite Element (FE) analyses were performed on a single pre-stressed curved beam with different material models. The same dimensions were used as for the Euler-Bernoulli beam model, listed in Table 1. First, an isotropic material model was used with a Young's modulus of 156 GPa and a Poisson ratio of 0.28 and a 3D FE analysis was carried out. Then, to capture the orientation dependent nature of the material properties of the cubic silicon lattice, an orthotropic material model was used with the values listed in Table 2. The model was rotated 45 degrees in counter clockwise direction to align the x-axis with the [110] direction, as is customary in a standard (100) silicon wafer (Hopcroft et al. [2]). Last, a 2D plane-stress model was made with the same orthotropic material model. Both 3D models used the SOLID186 (3D 20-node structural solid) element type and the 2D plane-stress model PLANE183 (2D 8-node structural solid) All models included geometric non-linearity.

1.3 Model comparison

Now, to evaluate the all previously described GAS models, in each model the beam was compressed incrementally whilst recording the stiffness in y-direction, yielding the plot in Figure 2. Of most interest were the results at 35 μm compression, and it could be observed that the 2D plane-stress model provided good accuracy for low computation power compared to the 3D model with orthotropic material properties. Therefore we decided to use it for all subsequent FE simulations. Also, both models that used the isotropic material predicted higher stiffnesses than the models that used the orthotropic material model. This indicated that the equivalent Young's modulus of 156 GPa of the isotropic material model did not seem to capture the orthotropic material properties well.

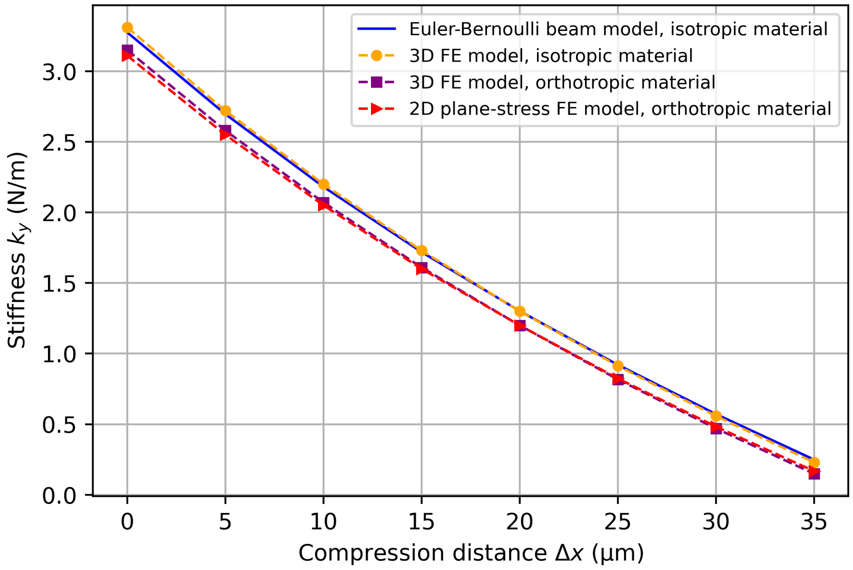

Figure 2: A comparison of the predicted stiffness of the GAS as a function of the compression distance by the numerical and FE models.

2 Estimating the spatial etch-offset gradient

In order to quantify the temperature effects that occur as a result of etch-offsets from manufacturing tolerances, first an estimate of the spatial distribution of these etch-offsets had to be obtained. This was done by using read-out capacitance data that was available for two wafers containing (the newer version) G7 chips. The differences in the read-out capacitance values from their nominal values served as a measure for the amount of over- and under-etching across each wafer. Figure 3 displays the location of the four read-out capacitors, grouped under the two capacitances C_L and C_R.

The nominal value of the capacitance for one side was calculated using the standard formula for the capacitance of a parallel plate capacitor with N finger-pairs:

$$C_{\mathrm{nom}} = 2\varepsilon_0 td(\frac{1}{g_1} + \frac{1}{g_2})N, \tag{12}$$

where ε_0 is the vacuum permittivity, t is the (out-of-plane) finger thickness, d is the finger overlap distance and g_1 and g_2 are the initial gap distances.

Due to the presence of a relatively large bias both between the left and right capacitances as well as between these and the nominal capacitance value, a parasitic capacitance value was added correct for this, equal to the difference between the median capacitance of each side for each wafer and the nominal capacitance $\mathrm{C_{nom}}$. The values are listed in Table 3.

Table 2: Orthotropic material properties of a standard silicon (100) wafer with the axes of the frame of reference [100],[010] and [001], from Hopcroft et al. [2].

Elastic property	Value
$\mathrm{E_x}$, $\mathrm{E_y}$, $\mathrm{E_z}$	165.7 GPa
ν_{yz}, ν_{zx}, ν_{xy}	0.28
$\mathrm{G_{yz}}$, $\mathrm{G_{zx}}$, $\mathrm{G_{xy}}$	79.6 GPa

CONFIDENTIAL

Figure 3: The read-out capacitors of the G7 chip

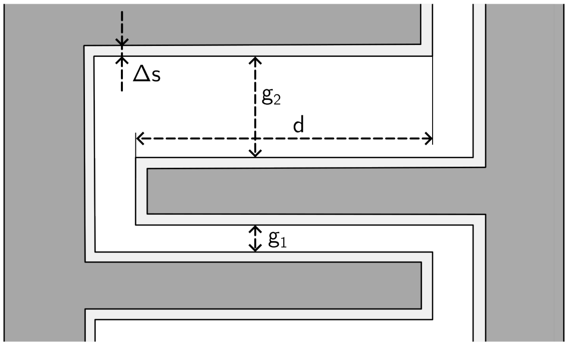

Figure 4: A schematic view of the etch-offset for the read-out sensing combs. The nominal dimensions are displayed in light grey and the effect of a positive etch-offset is displayed in dark grey.

With these parasitic capacitances, the following equation was solved for the etch-offset value Δs for each die:

$$C_{ijk} = 2\varepsilon_0 t(d - 2\Delta s_k)(\frac{1}{g_1 + 2\Delta s_k} + \frac{1}{g_2 + 2\Delta s_k}) + C_{ij,parasitic}, \tag{13}$$

where i and j indicate the wafer number and the side (left of right) respectively, and k indicates the die number. In Figure 4 the etch-offset for a positive Δs is schematically depicted.

The results for each die on the two wafers are depicted in Figure 5. Note that index x is the index of one die half. Calculating the gradient of the etch-offset values in both x and y directions for neighbouring dies then yielded Figure 6. From the occurrence of the etch-offset gradients it became apparent that most gradients were below 0.1 μm/die, and thus a maximum for the spring width variation across one die was set to be 0.2 μm.

Name	C_{nom}	C_{1L}	C_{1R}	C_{4L}	C_{4R}
Nominal capacitance (pF)	11.79	-	-	-	-
Median capacitance (pF)	-	13.97	13.56	13.74	13.32
Parasitic capacitance (pF)	-	2.18	1.77	1.95	1.53

Table 3: An overview of the measured capacitances and their parasitic correction values

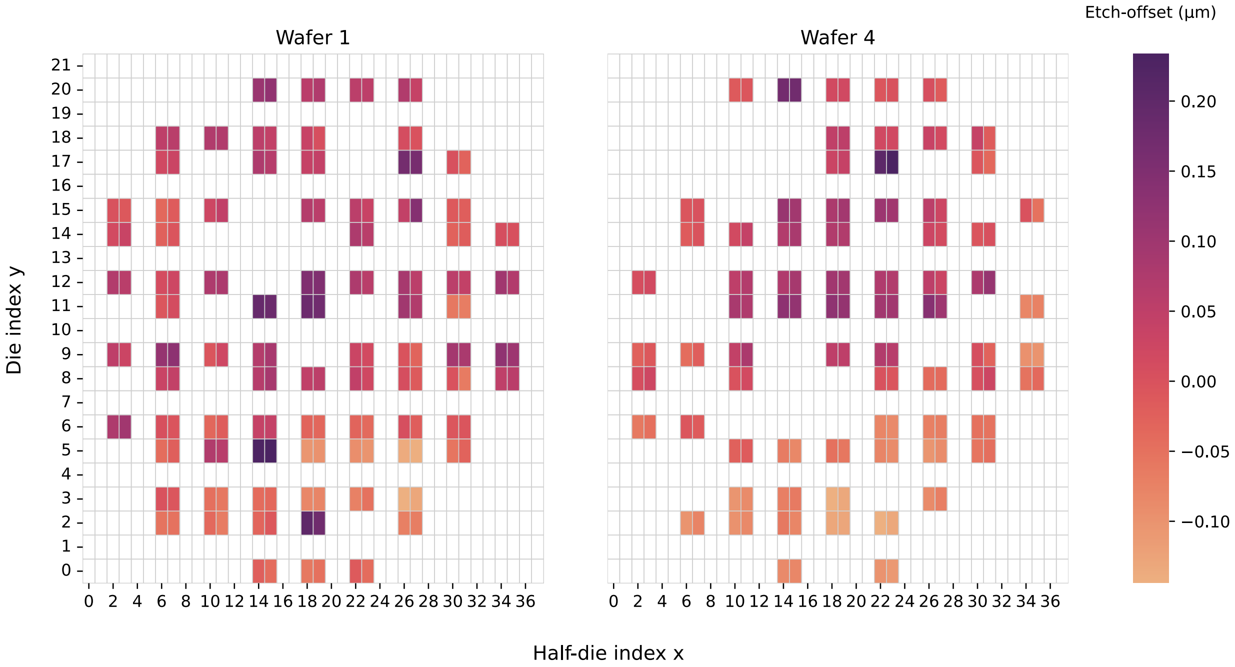

Figure 5: A contour plot showing the etch-offset distribution throughout two wafers based on the read-out capacitance data.

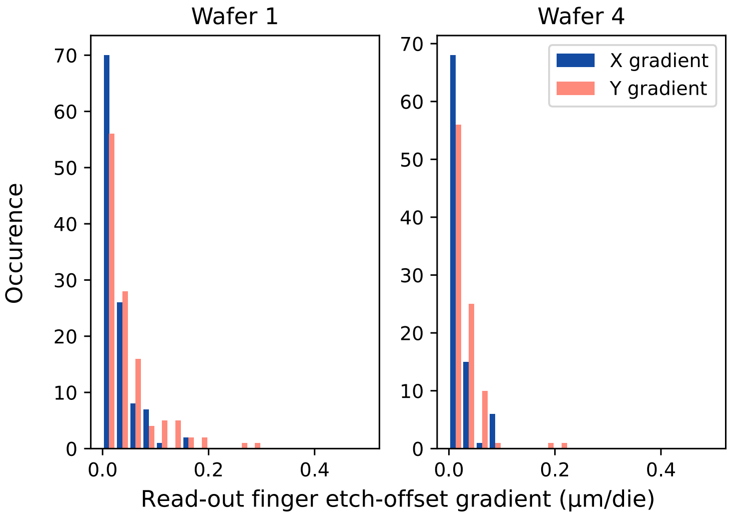

Figure 6: A histogram of the die-to-die etch-offset gradient for each wafer.

3 Modelling the thermal drift of bias

The temperature dependent drift of bias of the Innoseis MEMS accelerometer version G6 was modelled both numerically using the numerical model from in Section 1.1, as well as using 2D FE analysis in ANSYS Mechanical R2022. In both cases only in-plane effects were considered and bilateral symmetry was assumed around the sensing y-axis.

3.1 Numerical model

Plotting the restoring force F_R as a function of the spring width difference between the top and bottom springs for different compression distances of the top springs using the numerical model yielded Figures 7a to 7f.

Inspecting the plots became apparent that for each different compression distance of the top springs a minimum could be identified of the TDB where the lines for the different temperatures would seem to intersect. To verify this phenomenon a FE model was subsequently made.

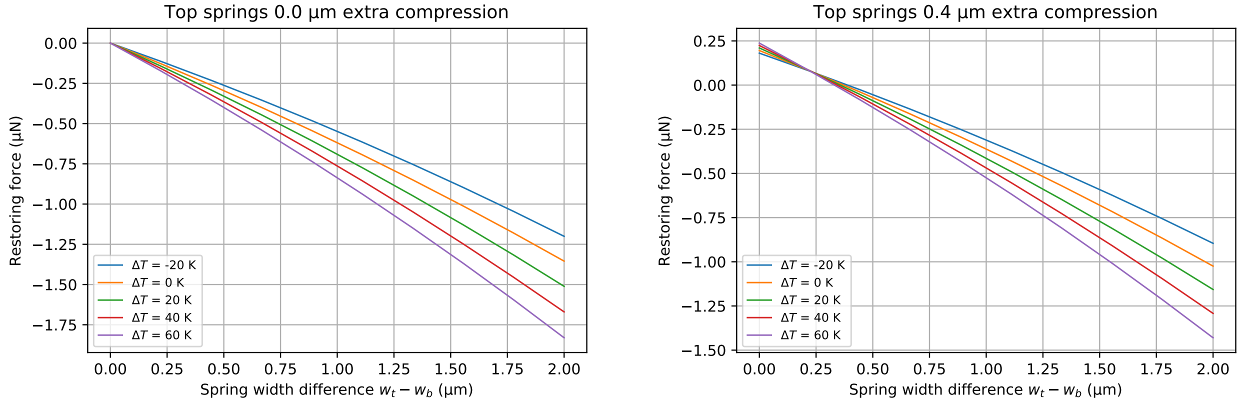

(a) Top springs 35.0 μm compressed.

(b) Top springs 35.4 μm compressed.

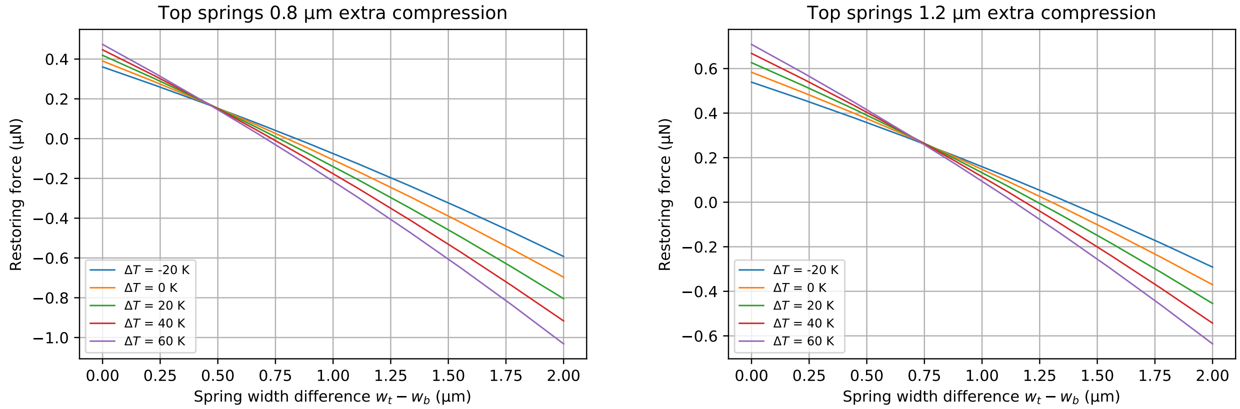

(c) Top springs 35.8 μm compressed.

(d) Top springs 36.2 μm compressed.

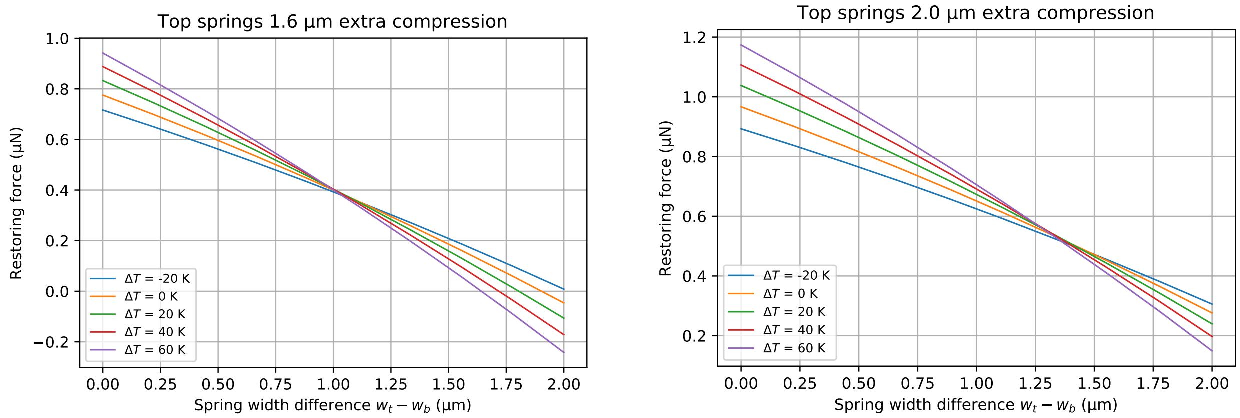

(e) Top springs 36.6 μm compressed.

(f) Top springs 37.0 μm compressed.

Figure 7: The temperature dependence of the restoring force for the numerical model with the isotropic material model as a function of spring width difference for different compression distances of the top springs. The bottom springs were always compressed 35.0 μm.

3.2 Finite Element model

3.2.1 Mesh convergence study

In Figure 8 the convergence of the restoring force F_R as a function of the amount of elements is shown. For this convergence study we used a perfectly symmetrical model of the accelerometer, therefore expecting a restoring force of zero. This allowed us to evaluate the progression in the mesh convergence, as any non-zero restoring force would likely be the result of an inaccuracy from the mesh. From the figure, after using more than 1M elements, we still observed a restoring force in the order of 10 nN. Because this was in the order of magnitude of the bias drift, we decided to exaggerate the etch-offset by factor 10 to obtain a larger bias drift, thereby reducing this mesh convergence error.

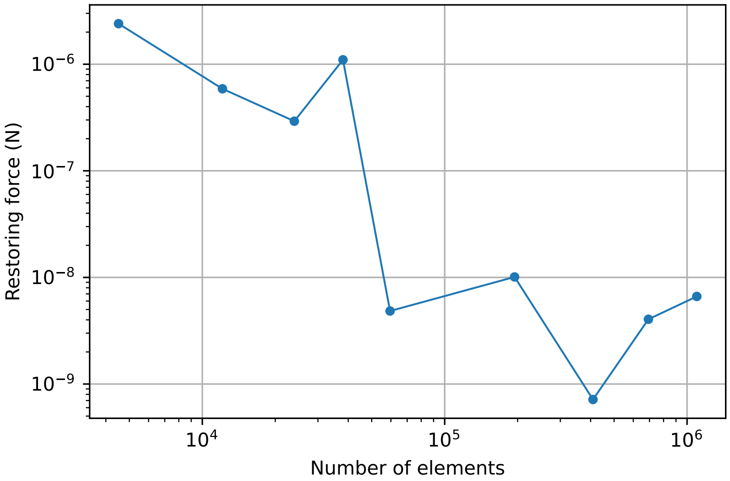

Figure 8: A plot showing the mesh convergence of the restoring force for equal top and bottom spring width and compression.

Again, plotting the restoring force F_R as a function of the spring width difference between the top and bottom springs for different compression distances of the top springs yielded Figures 9a to 9f. As was observed with the numerical model, for specific values of the top spring compression distance there appeared a minimum in the TDB at certain spring width differences.

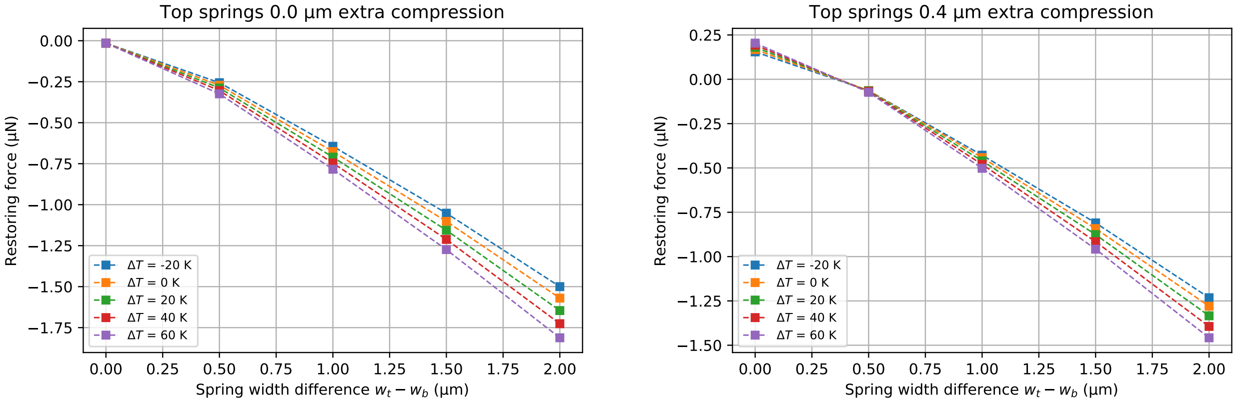

(a) Top springs 35.0 μm compressed.

(b) Top springs 35.4 μm compressed.

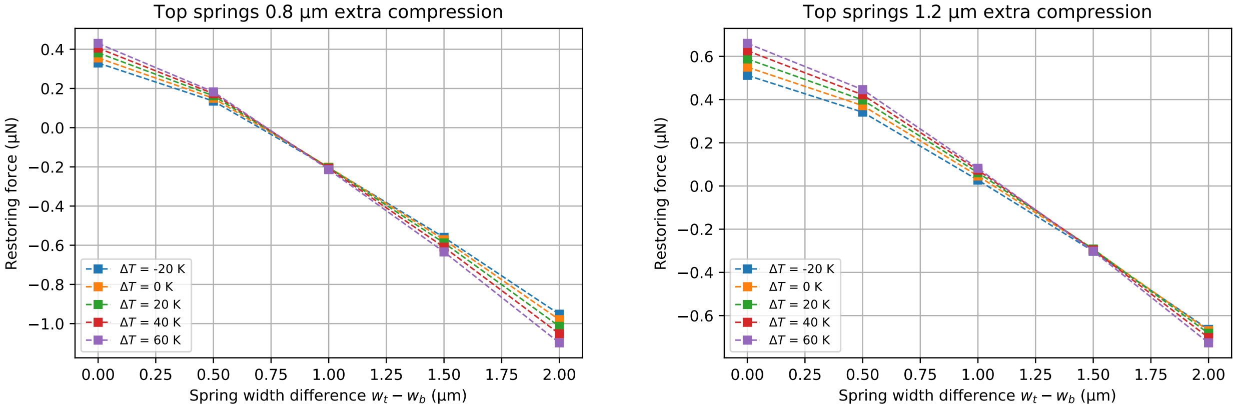

(c) Top springs 35.8 μm compressed.

(d) Top springs 36.2 μm compressed.

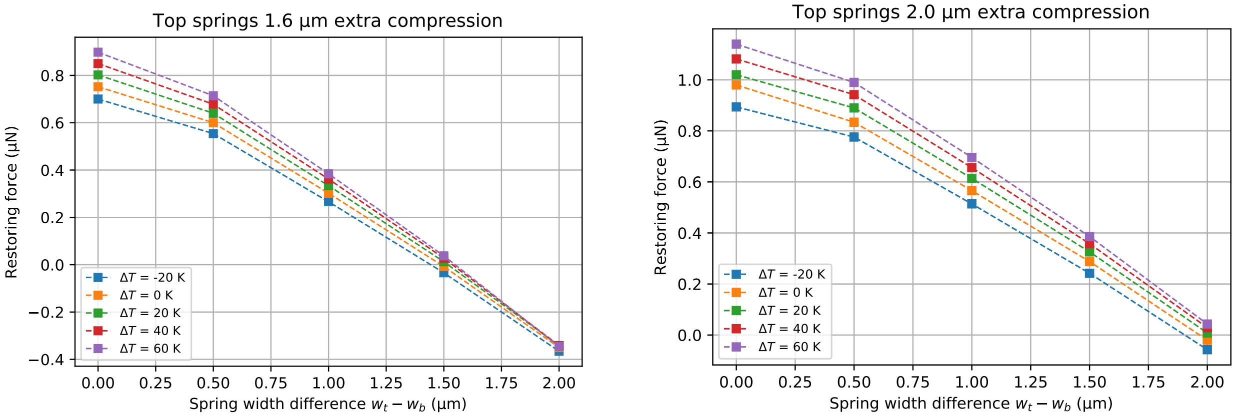

(e) Top springs 36.6 μm compressed.

(f) Top springs 37.0 μm compressed.

Figure 9: The temperature dependence of the restoring force for the FEA model with the orthotropic material model as a function of spring width difference for different compression distances of the top springs. The bottom springs were always compressed 35.0 μm.

4 Design process

4.1 Functional requirements, constraints and wishes

Based on the outcome of the TDB models the functional requirements were formulated. For each requirement, strategies that could fulfill it were generated, as well as its specific design specification. An overview of all requirements, strategies and specifications can be found in Table 4. Several constraints were also formulated, listed in Table 5.

Last, to determine the quality of the concepts that would be generated we formulated five criteria in the form of wishes that can be found in Table 6. With 'simple' in wish W3 we mean the estimated difficulty of designing the concept regarding the complexity of modelling.

Table 4: A tabular overview of the functional requirements and strategies.

Requirement	Strategy	Specification
R1. Provide a linear range of motion to the shuttle	Straight-line compliant mechanism that pushes the pawl in the direction of compression	400±40 nm
	Straight-line compliant mechanism that pushes the pawl towards the shuttle	2000±200 nm
R2. Compress or decompress the GAS pairs plus the shuttle springs	Compressing by using thermal expansion	$\geq$22 mN
	Compressing by using electrostatic force	$\geq$22 mN
	Compressing by using piezoelectric force	$\geq$22 mN
	Compressing by using electromagnetic force	$\geq$22 mN
	Compressing by using the gravitational force of the proofmass	$\geq$22 mN
	Decompressing by disengaging a ratchet mechanism	*unknown*
R3. Provide an adjustable extra compression distance of the GAS pairs without requiring a continuous energy supply	Ratchet mechanism	8 steps of 50±5nm
	Multi-stable mechanism	8 steps of 50±5nm
R4. Provide linear motion attenuation between the ratchet and the shuttle output displacement steps*	Lever-amplification principle	200/n ±10% where n is the number of ratchet-pawl pairs.
	Triangle-amplification principle	200/n ±10% where n is the number of ratchet-pawl pairs.

Table 5: A list of all constraints and their specifications that the design must adhere to.

Constraint	Specification
C1. The mechanism must fit on the Innoseis accelerometer version G6	See the footprint image
C2. The mechanism must be able to be manufactured using the current Innoseis manufacturing process	Minimal beam width: [CONFIDENTIAL] Minimal pattern spacing: [CONFIDENTIAL] Minimal feature size: [CONFIDENTIAL] Device layer height: [CONFIDENTIAL]
C3. The mechanism should be operable in a high-vacuum	[CONFIDENTIAL]
C4. The mechanism should not impair the operation of the accelerometer	
C5. The maximum principal tensile stress in the mechanism may not exceed a certain value	900 MPa
C6. In slender beams, the longitudinal force must be removed a certain factor from the critical buckling load	Factor of safety: 3
C7. The (out-of-plane) sag at any point must not be more than a certain value	5 μm

Table 6: A list of all the wishes used to grade each concept.

Wishes
W1. The device should be compact
W2. The device should have a linear input-output relation
W3. The device should be simple/not complex
W4. The dimensions of the device should be adjustable
W5. The device should be suitable for implementation into the Innoseis accelerometer version G7

4.2 Morphological chart

Based on the requirements from the previous section, we came up with solutions for the most feasible strategies that were also in line with the constraints from Table 5. These solutions are depicted in Figure 10 in the form of a morphological chart, where each row contains all the solutions for the sub-function of that row.

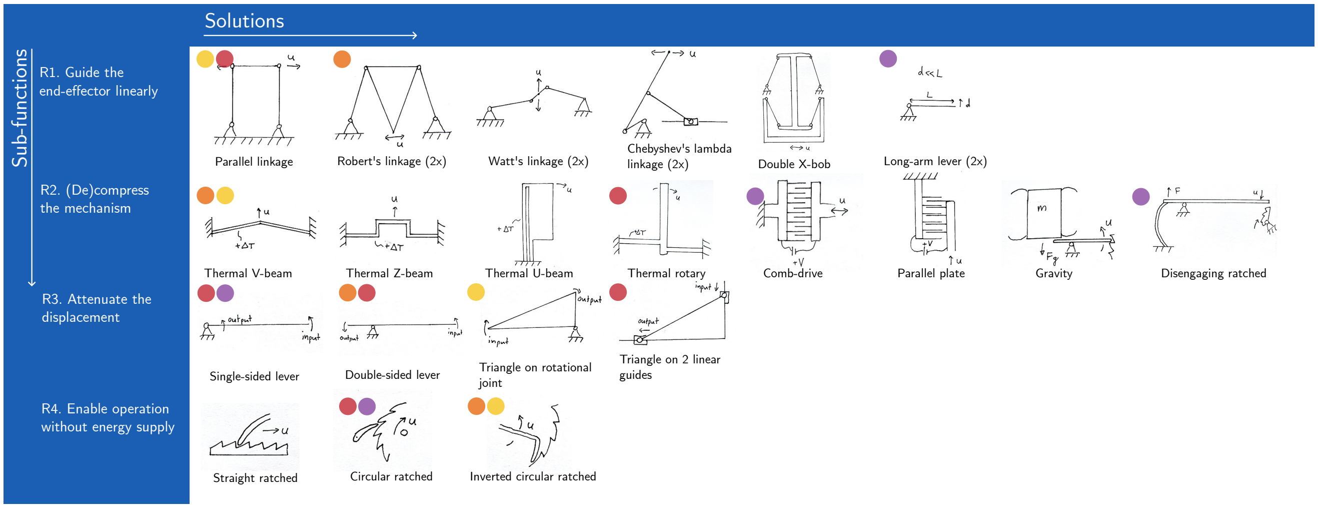

Figure 10: The morphological chart containing the sub-functions and solutions in each row. The colored dots represent the combinations of solutions that were evaluated as concepts.

4.3 Concept generation

In order to get a complete picture of the design possibilities that exist, solutions from different sub-functions that could work well together were combined to yield a total of four concepts. These combinations of solutions are indicated by the colored dots in Figure 10. Next, we worked out these concepts in the form of pencil drawings on top of an image of the available footprint to get a better feeling for the feasibility of each concept. This is shown in Figures 11a to 11d. For the size of the electrothermal actuators only the maximum displacement without an applied load was used since the true load was still unknown and hard to estimate. The formula to calculate the maximum displacement of the V-beam actuator was adopted from [3] :

$$\Delta y \approx \frac{\alpha L \Delta T}{\theta}, \tag{14}$$

where α is the (secant) coefficient of thermal expansion (2.6 ppm/K), L is the length of each beam, ΔT is the average increase in beam temperature and θ is the beam inclination angle. For 400 μm long beams with an average temperature increase of 350 K (adopted from [1]) and an inclination angle of 2°, this yielded a displacement of 12 μm. For the thermal rotary actuator in Concept 2 the elongation was calculated considering only the thermal expansion: $\Delta L = \alpha \Delta T L$. The actuation force of the comb-drive actuator from Concept 3 was roughly calculated as a function of the applied voltage ΔV. When the ratchet would be ~300 μm removed from the rotational joint that allows it to rotate, the angle it would have to rotate in order to traverse 8 steps of 10 μm was calculated as follows: $\Delta\phi = 8 \cdot 10/300 = 0.26$ rad (15.3°). Next we obtained an estimate of the moment that would be required to displace the ratchet this amount, assuming the rotational joint is a small-length flexure with constant rectangular cross-section. Using an expression for the torsional stiffness $K = EI/L$, where E is the Young's modulus (169 GPa), I is the second moment of area around the out-of-plane axis for the rectangular cross-section and L is the length of the flexure, this yielded, for a 50 μm long, 6 μm wide and [CONFIDENTIAL] μm thick flexure, a moment of $1.6 \cdot 10^{-6}$ N/m. The moment that the comb-drive can generate was now derived to be:

$$T = \frac{\varepsilon t N \Delta V^2 s}{y_0}, \tag{15}$$

where ϵ is the permittivity of free space (8.85 pF), t is the out-of-plane thickness ([CONFIDENTIAL]), N is the number of finger pairs, s is the distance from the comb-drive centre to the rotational flexure (the approximate moment arm) and y_0 is the gap size between the fingers. For a total comb-drive length of 800 μm and a finger-pitch of 25 μm, this meant that N would be 32. Then, using $s = 400$ μm, the expression for the moment equated to T = $7.25 \cdot 10^{-11}$ $\mathrm{Nm^{-1}V^{-2}}$. Therefore to achieve $1.6 \cdot 10^{-6}$ N/m the applied potential difference would need to be around 150 V.

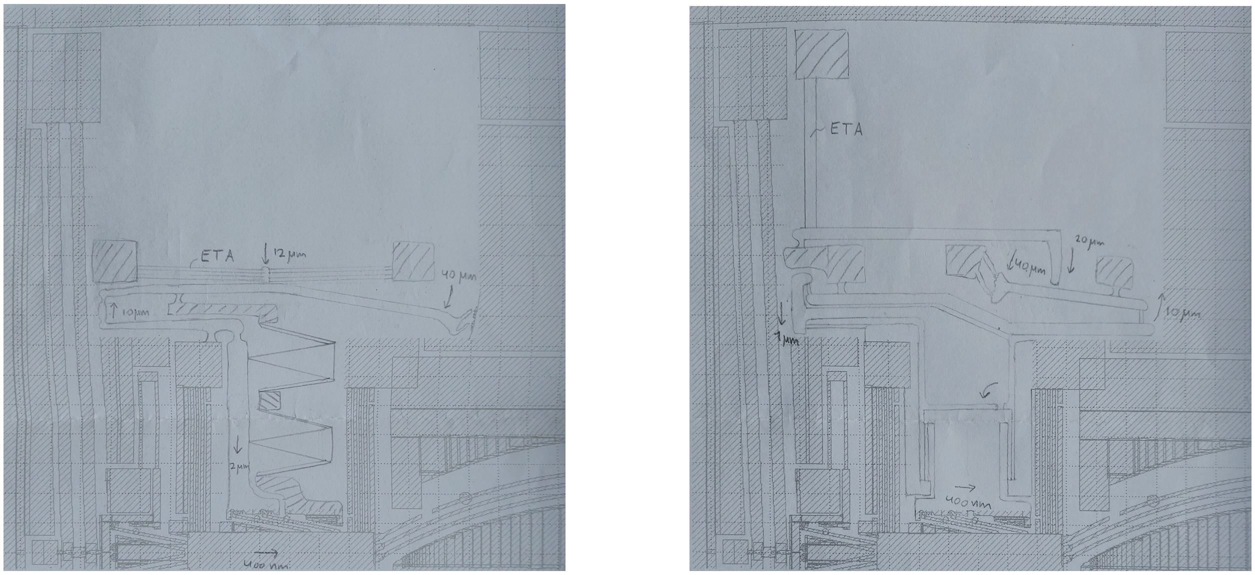

(a) Concept 1 (orange)

(b) Concept 2 (red)

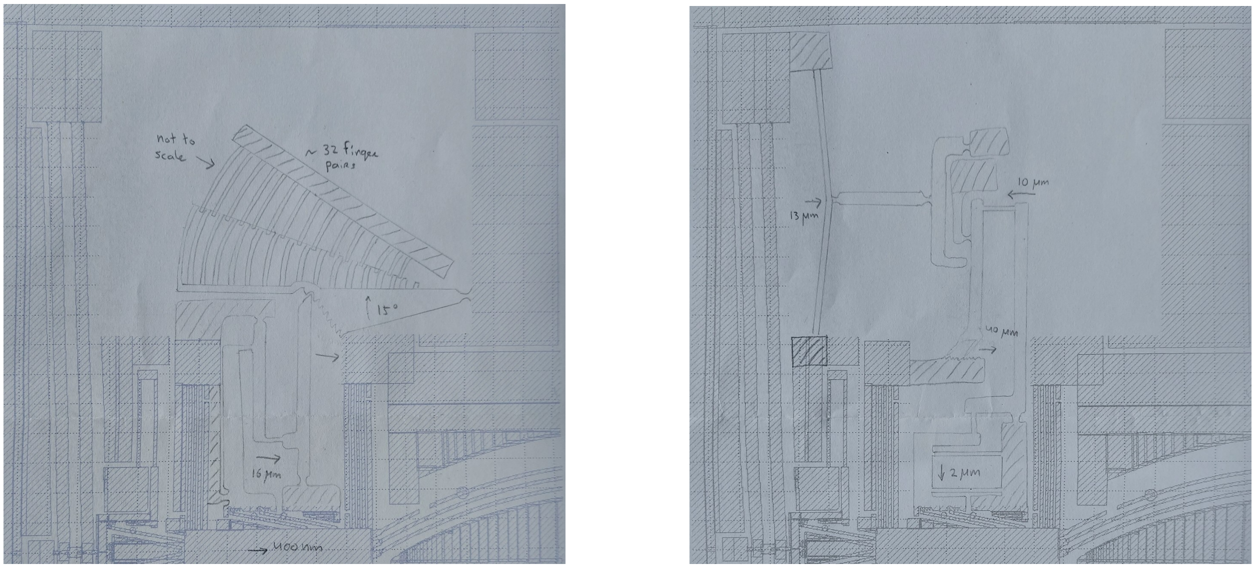

(c) Concept 3 (purple)

(d) Concept 4 (yellow)

Figure 11: An overview of the four concepts that were generated using the morphological chart.

Table 7: Scoring table for the concept wishes.

	Compact	Linear input-output	Simple/not complex	Adjustable	G7 implementation	**Sum**
Compact		-	-	+	+	2
Linear input-output	+		+	+	+	4
Simple/not complex	+	-		+	+	3
Adjustable	-	-	-		+	1
G7 implementation	-	-	-	-		0

4.4 Concept selection

In order to obtain a measure for the expected performance of each concept, we compared all the wishes with each other through Table 7, where a '+' was inserted in a cell when the wish from that row was deemed more important than the wish from that column, and a '-' was assigned otherwise. This yielded an ordering of the wishes from least to most important, after which we assigned weights to each wish to further indicate the relative importance. The list of wishes including their weights can be found in Table 8. After the concepts were roughly worked out by drawing them on paper, we then graded each one on a scale of 1 (poorest) to 5 (best) for each wish and multiplied it with the weight of that wish. For wish W2 concepts 1 and 3 were given four points because the arms that the pawls connect to (that need to displace at least 40 μm) were long and non-linearity in the conversion between translating and rotating motion could therefore be small. Concepts 2 and 4 scored only two points because that same arm was shorter, resulting possibly in a stronger non-linearity. Regarding simplicity (W3), concept 2 scored best (four points) due to its simple actuator. Concept 3 was given only one point because we estimated that the large floating comb-drive arm could potentially sag under the influence of gravity. Also, the disengaging ratchet mechanism might be more difficult the design because it is uncertain whether the pawl would be pressed into the ratchet by the force from the shuttle springs and GASs. Concepts 1 and 4 were given an average grade (three points) as they were judged to be more complex than Concept 2 because of the V-beam actuators, but less complex than Concept 3 for they utilized a conventional ratchet-pawl mechanism. On wish W1 (compactness) Concept 3 was given only one point because of the footprint that the comb-drive would occupy. The other concepts were all given the average grade of three points. The most adjustable (W4) we judged concept number 4, mostly because of the relatively larger space available to extend the inner links. The other concepts did not have this space and were therefore given a score of two points. Last, Concept 4 scored best on the potential to be implemented into accelerometer version G7 due to the vertical alignment of its links, for version G7 has less wide (x-direction) footprint areas F1 and F2. Concepts 1 and 2 have a horizontal alignment thus scoring only one point and Concept 3 scores marginally better thanks to its narrowly placed vertical links. The outcome of all the scores can be found in Table 9.

With the concept scores now established, a new concept was drawn to form a combination of the best solutions from each concept. Concept 1 and 4 received the highest overall scores of 90 and 86 respectively and was therefore chosen as the basis for the new concept. The V-beam thermal actuator, the circular ratchet and the down-pressing of the shuttle pawl formed the starting point. To vertically align the links, the downward y-axis motion had to be converted to an x-axis motion, and the triangular attenuation mechanism from Concept 2 was estimated to serve this purpose well as it could also form the first attenuation step. Last, more attenuation was added in the form of a double-sided lever to make the design more compact. The resulting design is schematically shown in the paper under section 'Preliminary design'.

Table 8: The listed wishes with their respective weights.

Wishes	Weight
W1. The device should be compact	5
W2. The device should have a linear input-output relation	10
W3. The device should be simple/not complex	8
W4. The dimensions of the device should be adjustable	4
W5. The device should be suitable for implementation into the Innoseis accelerometer version G7	3

Table 9: The concepts graded on each wish, yielding a weighted total score.

		Concept 1		**Concept 2**		**Concept 3**		**Concept 4**	
Wish	Weight	Grade	Score	Grade	Score	Grade	Score	Grade	Score
W2. Linear input-output relation	10	4	40	2	20	4	40	2	20
W3. Simple/not complex	8	3	24	4	32	1	8	3	24
W1. Compact	5	3	15	3	15	1	5	3	15
W4. Adjustable	4	2	8	2	8	2	8	3	12
W5. G7 implementation	3	1	3	1	3	2	6	5	15
Total score			**90**		**78**		**67**		**86**

4.5 Dimensioning, phase 1

4.5.1 Buckling hand-calculation of the flexures with length L_1

In order to calculate the axial forces in the flexures with length L_1, we first had to obtain the force of the shuttle pawl on point U. This was done using the numerical GAS model from Section 1.1 and the PRB model of the three pairs of shuttle springs. For a compression distance Δx_i of 35 μm, this yielded roughly 22 mN in x-direction. It was then assumed that the force in the shuttle pawl would be in the axial direction, therefore resulting in an additional force in y-direction of 4.4 mN (22 mN $\cdot$ tan(11.3°), 11.3° is the shuttle pawl angle with the x-axis). Next, a drawing was made to derive the static equilibrium of the forces and moments, shown in Figure 12. It was assumed that the moments in points D' and B' could be neglected, as well as the y-component of the reaction forces because we expected that most of force $F_{\mathrm{U,y}}$ would be compensated by $F_{\mathrm{E,y}}$. Similarly, the x-component of the reaction force in point E' was neglected as we expected it to be mainly compensated by forces $F_{\mathrm{D',x}}$ and $F_{\mathrm{B,x}}$. We also neglected the moment in point E' as its exacty value could not yet be determined. Writing down the force equilibrium equations and the moment equilibrium equation around point D' now yielded:

$$\xrightarrow{+} \Sigma F_x = 0: \quad -F_{\mathrm{U,x}} + F_{\mathrm{D',x}} + F_{\mathrm{B',x}} = 0, \tag{16}$$

$$+\uparrow \Sigma F_y = 0: \quad -F_{\mathrm{E,y}} + F_{\mathrm{U,y}} = 0, \tag{17}$$

$$+\circlearrowleft \Sigma M_{\mathrm{D'}} = 0: \quad dF_{\mathrm{E',y}} + aF_{\mathrm{B',x}} - (a+b)F_{\mathrm{U,x}} - cF_{\mathrm{U,y}} = 0. \tag{18}$$

The arrows indicate here the positive directions. Inserting the dimensions for b,c and d and solving Equations 17 and 18 resulted in $F_{\mathrm{B',x}} = (9.7 \cdot 10^{-7} + 22 \cdot 10^{-3}a)/a$. Euler's buckling formula was now used ($F_{\mathrm{buckle}} = \pi^2\, EI/L^2$) with a Young's modulus of 169 GPa given a flexure length L_1 of 180 μm with a width of 6 μm, yielding a buckling limit of 92.7 mN. Equating the buckling limit divided by three (constraint C6) with the answer for $F_{\mathrm{B',x}}$ then gave a lower limit for length a of 109 μm. In this case force $F_{\mathrm{D',x}}$ would be negative according to Equation 16 and therefore free from the risk of buckling. Due to the availability of footprint and the uncertainty on the moment of point E' we decided to give length a the largest possible value of 230 μm, being only limited by the motion of the attenuation stage pawls at point Z.

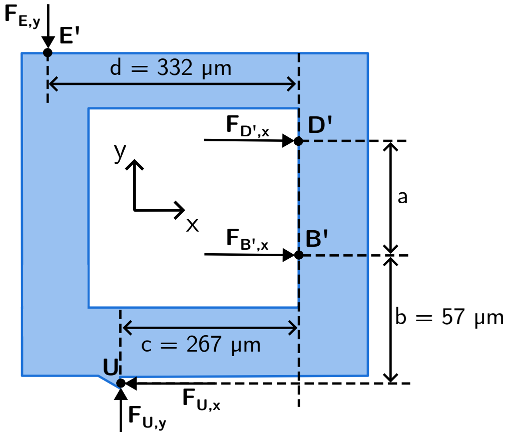

Figure 12: A schematic illustration of all the forces that were considered in the buckling hand-calculation.

4.5.2 Dimensioning the ETA

In Figure 13 all contour plots can be seen that were used for determining the most promising configuration of the ETA. To obtain the largest displacement (and therefore the lowest force on flexures O and N) we selected a beam width of 15 μm. A beam angle θ_{ETA} of 3.7° seemed to give the largest safety margins on the buckling constraint (pink curve) and the temperature constraint (red curve), and was therefore selected.

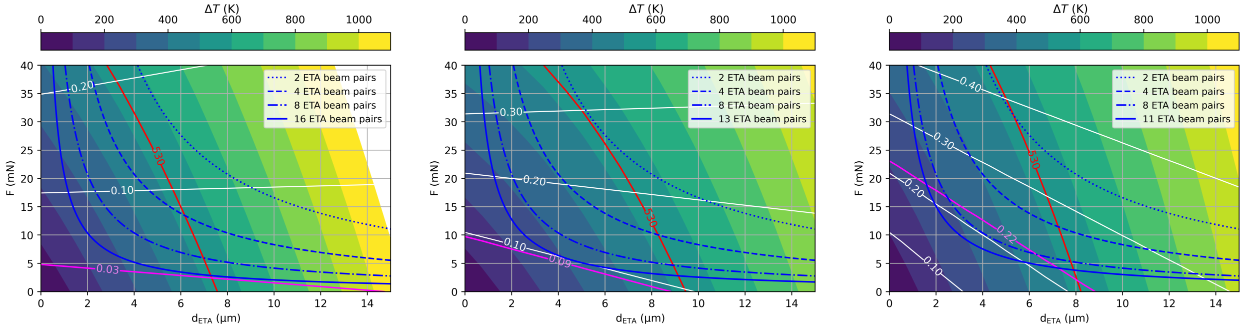

(a) Beam width w_{ETA}: 10 μm, beam angle θ_{ETA}: 5°

(b) Beam width w_{ETA}: 15 μm, beam angle θ_{ETA}: 3°

(c) Beam width w_{ETA}: 20 μm, beam angle θ_{ETA}: 3°

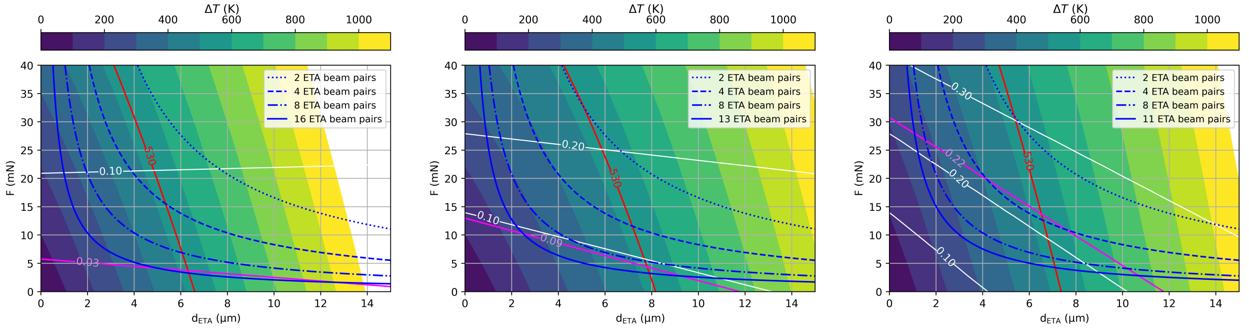

(d) Beam width w_{ETA}: 10 μm, beam angle θ_{ETA}: 6°

(e) Beam width w_{ETA}: 15 μm, beam angle θ_{ETA}: 4°

(f) Beam width w_{ETA}: 20 μm, beam angle θ_{ETA}: 4°

Figure 13: Contour plots of the average temperature difference in the ETA beam pairs as a function of the displacement of the ETA shuttle d_{ETA} and the applied force F. The red curve indicates the temperature constraint, the magenta line indicates the buckling constraint of the ETA beams and the blue curves indicate the points that provide the work required to fully compress the whole mechanism. The white curves indicate the longitudinal force P_0 in each ETA beam.

4.6 Dimensioning, phase 2

4.6.1 Temperature dependence of the thermal conductivity

To capture the temperature dependence of the thermal conductivity in our silicon wafer we estimated the data for our boron doping-level of $1.5 \cdot 10^{19}$ cm^{-3} from [4] and [5], see Figure 14.

4.6.2 Temperature dependence of the resistivity

For the temperature dependence of the resistivity we used the data from [6] as this was the only source we could find that reported data for higher temperatures, seen in Figure 15. We extrapolated the last data point (indicated by the star) in the direction of the intrinsic resistivity curve from [7], since it has been shown that, at high temperatures, the resistivities of doped silicon all fall on the same (intrinsic) line [8]. Resistivity data from [9] was also plotted as a verification of the data of [6].

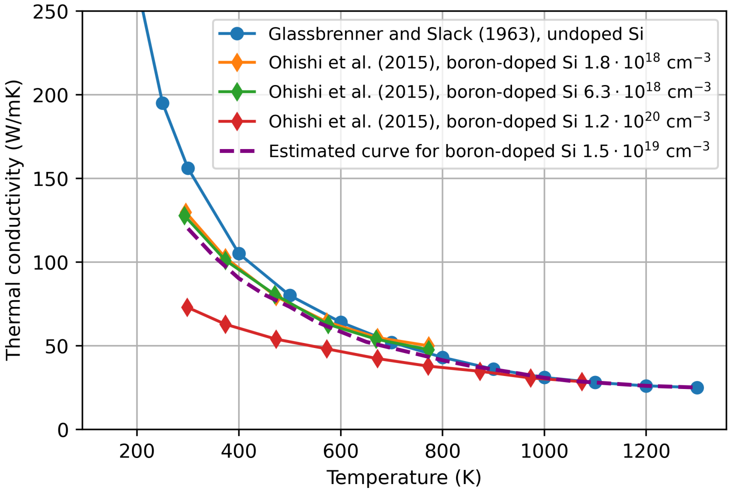

Figure 14: Thermal conductivity data for different doping levels as a function of temperature from [4] and [5], including the estimate for our doping level of $1.5 \cdot 10^{19}$ cm^{-3}.

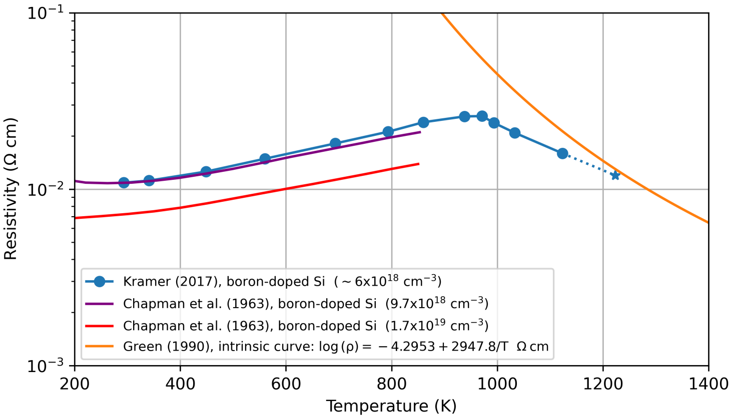

Figure 15: Resistivity data for different doping levels as a function of temperature from [4] and [5], including one estimated data point above 1200 K (blue star).

4.6.3 Validating the ETA models

The validation of the numerical and FE models was done using the experimental data from the in vacuum operated ETA developed by Zhu et al. [10]. By replicating their design and applying the average temperature data from [10, Fig. (11)] derived from resistance measurements, the outcome from our thermo-mechanical models could be compared to their measurements. For the thermo-electric FE model the current was used as the input parameter. Both models used PLANE183 elements (2D 8-node structural solid) and included geometric non-linearity.

The results are shown in Figure 16. The numerical thermo-mechanical model first overestimates the displacement up to roughly 5mA, then shows an underestimation up to roughly 14mA after which the model again overestimates the data. The FE thermo-mechanical model shows a similar comparison although the overestimation for low currents is more severe while the subsequent underestimation is smaller. Also, the FE model starts to overestimate the experimental data again sooner compared to the numerical model. The FE coupled model shows the best agreement with the data, although, at high currents, it seems to follow a less steep of a trajectory.

The observation that both the numerical and FE thermo-mechanical model show the same characteristic in the deviation from the experimental data could suggest an inaccuracy in the derivation of the average temperature from the measured resistance. Despite the observed deviations, overall the models seemed to predict the experimental data reasonable well and we accepted to use them in the dimensioning of our own ETA.

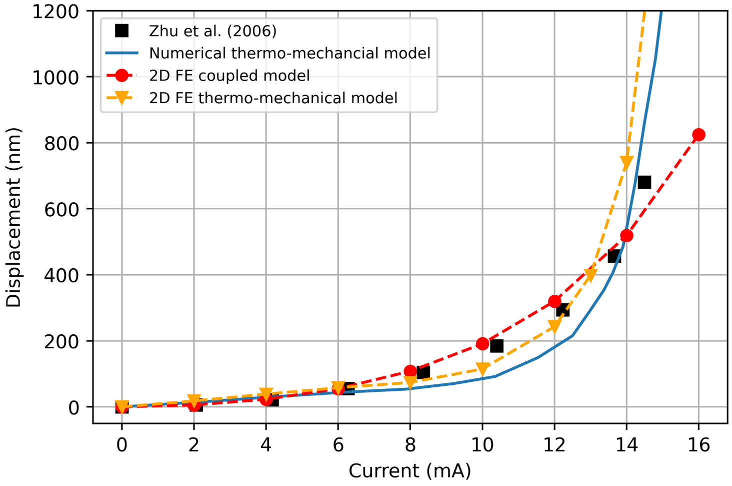

Figure 16: A plot showing how well the models predict the experimental data of the ETA from [10].

4.6.4 Mesh convergence

The mesh convergence of the stress for the three models (segment O-U, segment U-shuttle and the ETA) can be seen in Figure 17.

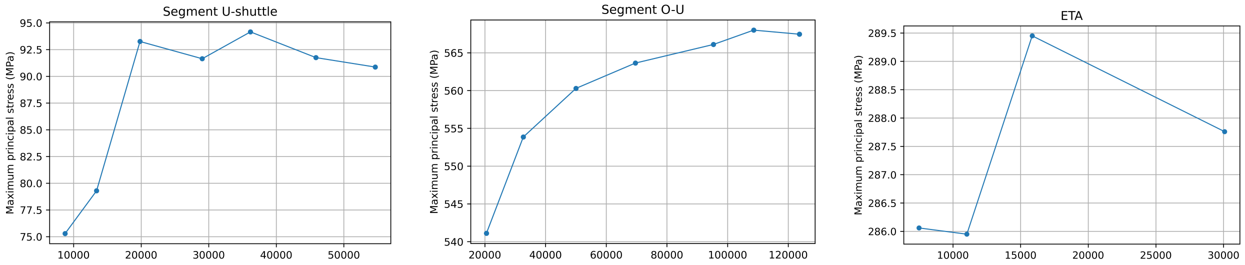

(a) (b) (c)

Figure 17: Three mesh convergence plots: (a) for segment U-shuttle, (b) for segment O-U and (c) for the ETA.

5 Results

5.1 Verifying the attenuation stage pawl deformation

Since the displacements of the attenuation stage pawls and shuttle were measured by displacing point O, the results might not represent the case where the pawl would rest on the ratchet-teeth. To get an estimate of the error this could give in our measurement, we did force-displacement measurements (forward and backward) with the load cell and linear stage at the connection point of the attenuation stage pawls, indicated by the red arrows in Figure 18. For this measurement the pawl was placed on the first ratchet-tooth. The results can be viewed in Figure 19, where 10 measurements are shown. The average slope of the forward and backward curves was determined to be 15.1 N/mm using NumPy's `polyfit` function with degree set to 1. Taking the maximum normal force in point Y from the FE model (0.29 N) in combination with the average slope of these measurements (15.1 N/mm), the displacement of the connection points of the attenuation stage pawls relative to the pawl-end was estimated to be (0.29 N/15.1 N/mm =) 0.02 mm.

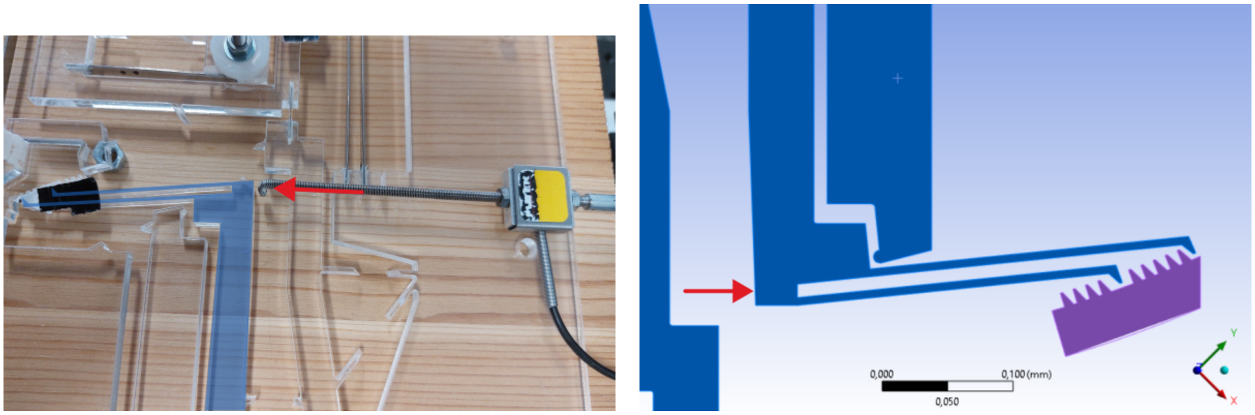

(a) A picture of the measurement set-up to measure the force-displacement of the loading of the attenuation stage pawl.

(b) An illustration indicating the point where the attenuation stage pawl deformation is measured with the red arrow.

Figure 18: Deformation measurement of the attenuation stage pawl.

5.2 Small-scale silicon design

Figure 20 shows the FE and PRB model data of the attenuation stage pawl displacement as a function of the ETA shuttle (point O) displacement for the small-scale silicon design.

5.3 Large-scale prototype

In Figure 21 the experimental and model (FE and PRB) data are shown of the attenuation stage pawl displacement as a function of the ETA shuttle (point O) displacement.

5.4 Finite Element modelling of the sag

The out-of-plane sag was investigated using a 3D FE model by applying standard earth gravity along the z-axis. We used 267k elements of type SOLID187 (3D 10-node tetrahedral structural solid) to ensure mesh convergence of the deformation below 1%, and the result can be viewed in Figure 22 where the maximum sag appears to be 0.24 nm.

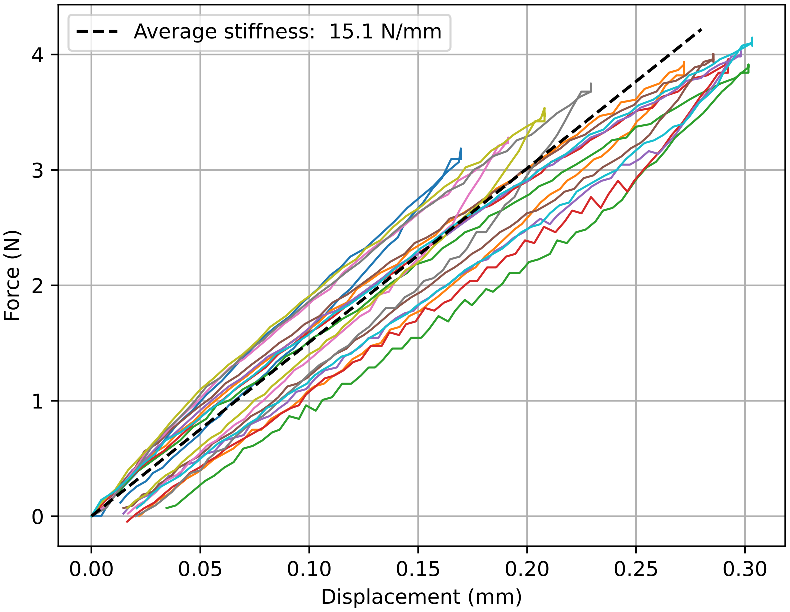

Figure 19: All 10 measurements of the force-displacement relationship at the attenuation stage pawl connection point.

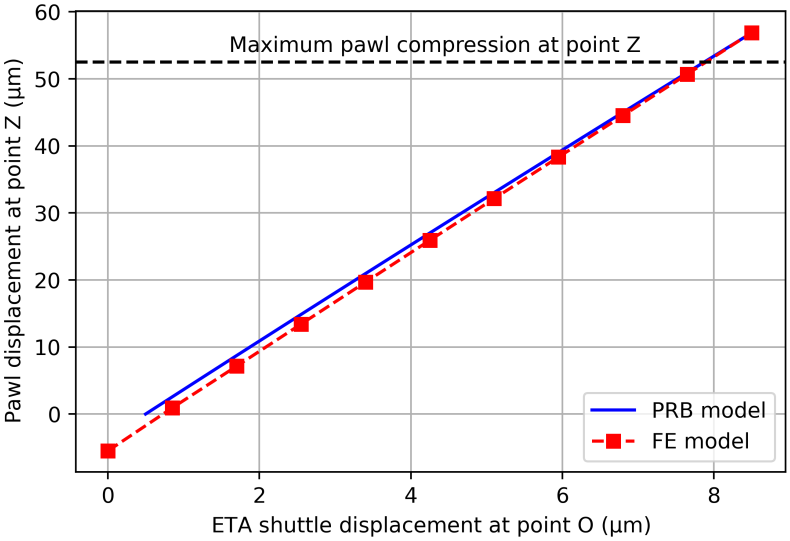

Figure 20: The attenuation stage pawl displacement plotted against the ETA shuttle displacement.

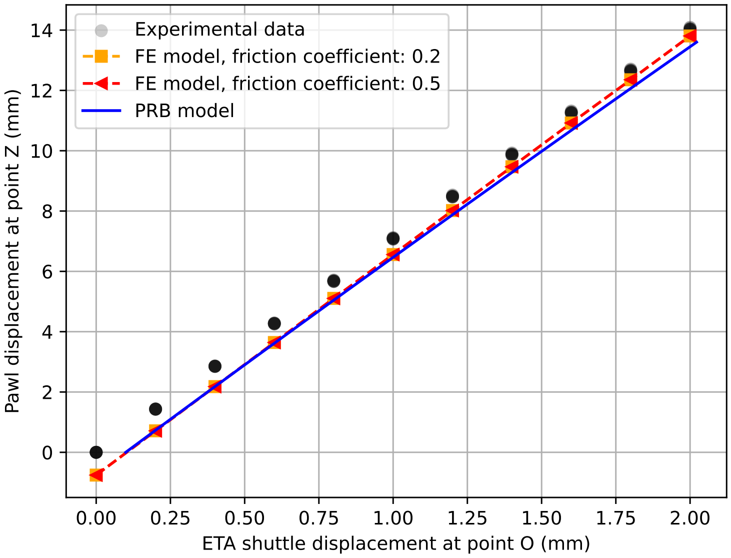

Figure 21: The attenuation stage pawl displacement at tracking point 1 plotted against the input displacement of the translation stage.

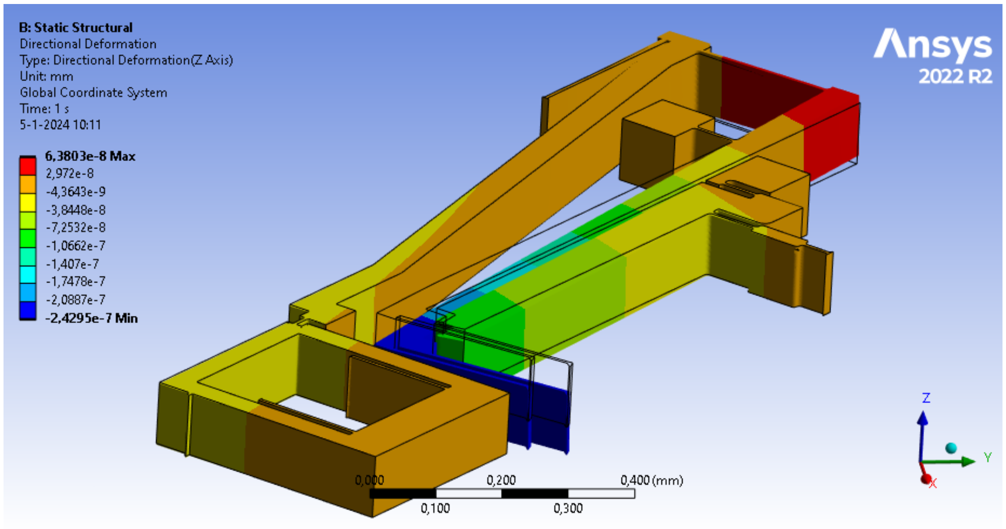

Figure 22: The out-of-plane (z-axis) sag of the mechanism according the the 3D FE model

References

[1] B. Boom, "Acceleration sensing at the nano-g level development and characterisation of low-noise microseismometers for next generation gravitational wave detectors," 2020.

[2] M. A. Hopcroft, W. D. Nix, and T. W. Kenny, "What is the young's modulus of silicon?" *Journal of microelectromechanical systems*, vol. 19, no. 2, pp. 229–238, 2010.

[3] J. Luo, A. Flewitt, S. Spearing, N. Fleck, and W. Milne, "Modelling and fabrication of microspring thermal actuator," 2004.

[4] Y. Ohishi, J. Xie, Y. Miyazaki, Y. Aikebaier, H. Muta, K. Kurosaki, S. Yamanaka, N. Uchida, and T. Tada, "Thermoelectric properties of heavily boron-and phosphorus-doped silicon," *Japanese journal of applied physics*, vol. 54, no. 7, p. 071301, 2015.

[5] C. J. Glassbrenner and G. A. Slack, "Thermal conductivity of silicon and germanium from 3 k to the melting point," *Physical review*, vol. 134, no. 4A, p. A1058, 1964.

[6] J. Kamer, D. E. Hennes, and R. Buning, "Characterizing the electrical and mechanical behavior of the electro-thermal actuators of the nikhef accelerometer mems design."

[7] M. A. Green, "Intrinsic concentration, effective densities of states, and effective mass in silicon," *Journal of Applied Physics*, vol. 67, no. 6, pp. 2944–2954, 1990.

[8] G. L. Pearson and J. Bardeen, "Electrical properties of pure silicon and silicon alloys containing boron and phosphorus," *Physical Review*, vol. 75, no. 5, p. 865, 1949.

[9] P. Chapman, O. Tufte, J. D. Zook, and D. Long, "Electrical properties of heavily doped silicon," *Journal of Applied Physics*, vol. 34, no. 11, pp. 3291–3295, 1963.

[10] Y. Zhu, A. Corigliano, and H. D. Espinosa, "A thermal actuator for nanoscale in situ microscopy testing: design and characterization," *Journal of micromechanics and microengineering*, vol. 16, no. 2, p. 242, 2006.